

The structure of L-rhamnulose-1-phosphate aldolase (class II) solved by low-resolution SIR phasing and 20-fold NCS averaging

Markus Kroemer and Georg E. Schulz*

Institut für Organische Chemie und Biochemie,
Albert-Ludwigs-Universität Freiburg,
Albertstrasse 21, 79104 Freiburg im Breisgau,
Germany

Correspondence e-mail:
schulz@bio.chemie.uni-freiburg.de

The enzyme L-rhamnulose-1-phosphate aldolase catalyzes the reversible cleavage of L-rhamnulose-1-phosphate to dihydroxyacetone phosphate and L-lactaldehyde. It is a homotetramer with an M_r of 30 000 per subunit and crystallized in space group $P3_221$. The enzyme shows a low sequence identity of 18% with the structurally known L-fuculose-1-phosphate aldolase that splits a stereoisomer in a similar reaction. Structure analysis was initiated with a single heavy-atom derivative measured to 6 Å resolution. The resulting poor electron density, a self-rotation function and the working hypothesis that both enzymes are C_4 symmetric with envelopes that resemble one another allowed the location of the 20 protomers of the asymmetric unit. The crystal-packing unit was a D_4 -symmetric propeller consisting of five D_4 -symmetric octamers around an internal crystallographic twofold axis. Presumably, the propellers associate laterally in layers, which in turn pile up along the 3_2 axis to form the crystal. The non-crystallographic symmetry was used to extend the phases to the 2.7 Å resolution limit and to establish a refined atomic model of the enzyme. The structure showed that the two enzymes are indeed homologous and that they possess chemically similar active centres.

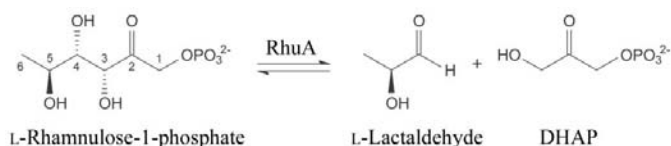
Received 10 January 2002
Accepted 11 March 2002

PDB Reference: L-rhamnu-
lose-1-phosphate aldolase,
1gt7, r1gt7sf.

1. Introduction

Aldolases come in two classes with different reaction mechanisms. Class I aldolases form a Schiff-base intermediate between the carbonyl C atom of the aldehyde and an essential lysine residue, whereas class II aldolases use a Zn^{2+} ion as an electron sink for the aldol condensation (Horecker *et al.*, 1972). Numerous structures of class I aldolases (Blom & Sygusch, 1997; Kim *et al.*, 1998; Dalby *et al.*, 2001; Wymer *et al.*, 2001) and three structures of class II aldolases (Dreyer & Schulz, 1993; Cooper *et al.*, 1996; Izard & Blackwell, 2000) have been established. Most of them contain a $(\beta\alpha)_8$ -barrel as the common structural motif. The chain fold of L-fuculose-1-phosphate aldolase from *Escherichia coli* (FucA, EC 4.1.2.17), however, differs greatly from the others. Moreover, it shows a rare C_4 -symmetric tetrameric state that is unique in this enzyme group.

L-Rhamnose (6-deoxy-L-mannose) is the most common deoxy hexose sugar and a component of various glycosides, polysaccharides and glycoproteins in bacteria, plants and animals. *E. coli* metabolizes L-rhamnose using a set of enzymes encoded in the L-rhamnose regulon, which consists of the L-rhamnose transport protein, L-rhamnose isomerase, L-rhamnulose kinase, L-rhamnulose-1-phosphate aldolase (RhuA; EC 4.1.2.19) and two regulatory proteins (Moralejo *et al.*, 1993). RhuA belongs to class II and catalyzes the cleavage

**Figure 1**

The reversible aldol cleavage/addition reaction catalyzed by L-rhamnulose-1-phosphate aldolase (RhuA). FucA uses L-lactaldehyde and DHAP to produce the 4-epimer L-fuculose-1-phosphate.

of L-rhamnulose-1-phosphate to dihydroxyacetone phosphate (DHAP) and L-lactaldehyde (Fig. 1). The reaction is reversible, so that the enzyme can be used as a catalyst for stereospecific carbon–carbon bond formation. Such reactions are attractive because they can be applied to the synthesis of carbohydrates and other chiral compounds (Bednarski *et al.*, 1989; Fessner *et al.*, 1991; Wong *et al.*, 1995). Like many DHAP-dependent aldolases, RhuA is highly specific for DHAP but accepts a wide range of aldehydes (Fessner & Walter, 1996). RhuA is a homotetramer in solution (Chiu & Feingold, 1969) and consists of 274 amino-acid residues per subunit with a calculated molecular mass of 30 149 Da (Moralejo *et al.*, 1993). Here, we report the structure of RhuA as determined in a very large unit cell using a single low-resolution heavy-atom derivative, density averaging and phase extension.

2. Materials and methods

2.1. Protein production and purification

Using a derivative of plasmid pKK223-3, the enzyme was produced in *E. coli* K12 strain JM105 under control of the *tac* promoter. The cells were grown at 310 K and pH 7.5 in 2 l Luria–Bertani medium containing 100 $\mu\text{g ml}^{-1}$ ampicillin to an OD_{578} of 0.8 and then induced for 12 h with 1 mM isopropyl- β -D-thiogalactopyranoside (IPTG). All further handling was at 277 K. Cells were harvested by centrifugation (Sorvall GS-3, 8000g, 20 min), resuspended in three volumes of buffer TMZ (20 mM Tris–HCl pH 7.2, 10 mM β -mercaptoethanol, 1 mM ZnCl_2) and then sonicated (model 7100, Measuring and Scientific). After centrifugation (Sorvall SS-34, 47 800g, 50 min), 0.1 ml 16% (w/v) Polymin-P pH 7.0 was added to the supernatant and after 30 min the solution was centrifuged again for 20 min under the same conditions.

The supernatant was loaded at a flow rate of 24 ml h^{-1} onto a DEAE-Sepharose Cl-6B column (Pharmacia) equilibrated with buffer TMZ. After washing with 100 mM NaCl in buffer TMZ, the protein was eluted at 240 mM NaCl using a linear NaCl gradient in buffer TMZ. The eluate was then precipitated by gradually adding ammonium sulfate to a final concentration of 1.7 M and separated by centrifugation (Sorvall SS-34, 47 800g, 10 min). The precipitate was dissolved in buffer HA (5 mM $\text{Na}_2\text{HPO}_4/\text{KH}_2\text{PO}_4$ pH 7.2, 5 mM β -mercaptoethanol, 1 mM ZnCl_2) and dialyzed three times against 1 l buffer HA. The enzyme was then loaded at a flow rate of 18 ml h^{-1} onto a hydroxylapatite column and subsequently eluted at 180 mM phosphate using a linear phosphate

gradient in buffer HA. The preparation resulted in about 100 mg RhuA per litre of culture.

2.2. Crystallization, heavy-atom derivative and data collection

Initial crystallization conditions were found by screening (Jancarik & Kim, 1991). The crystals grew reproducibly at 293 K in hanging drops containing 5 mg ml^{-1} protein, 5 mM of the enzyme inhibitor phosphoglycolohydroxamate, 0.9 M sodium formate, 5 mM β -mercaptoethanol, 0.5 mM ZnCl_2 and 0.1 M sodium acetate pH 4.6. The reservoir contained 1.8 M sodium formate, 5 mM β -mercaptoethanol and 0.1 M sodium acetate pH 4.6. After three months, the crystals reached dimensions of up to 500 \times 500 \times 350 μm . Co-crystallization with phosphoglycolohydroxamate improved the crystal quality. A similar improvement had been observed with FucA (Dreyer & Schulz, 1996a). A tantalum bromide derivative was obtained by soaking a native crystal for 2 h in 5 mM partially dissolved $\text{Ta}_6\text{Br}_{12}^{2+}$.

A native data set and a data set from the tantalum-cluster soak, each from a single crystal, were collected at room temperature on a rotating-anode generator (Rigaku, model RU-200B) equipped with a multiwire area detector (Bruker–Nicolet, model X-1000). The data were processed with XDS (Kabsch, 1988). A second native data set was collected at 100 K using synchrotron radiation (beamline X11 of the EMBL Outstation, Hamburg) with a MAR Research image plate. These data were processed with MOSFLM (Leslie, 1992). For cryoprotection, we added glycerol gradually to 20% (v/v). All data were scaled and reduced with SCALA (Evans, 1993).

2.3. Data analysis and refinement

The self-rotation function was calculated with POLARRFN (Collaborative Computational Project, Number 4, 1994) using data in the 8–6 \AA resolution range and outer and inner vector shell radii of 35 and 5 \AA , respectively. After scaling with SCALEIT (Howell & Smith, 1992), the initial tantalum-cluster site was located by a difference Patterson map at 6 \AA resolution and refined with MLPHARE (Collaborative Computational Project, Number 4, 1994), describing it as a single point scatterer with a *B* factor of 200 \AA^2 .

The resulting single isomorphous replacement (SIR) electron-density map was used in the search for non-crystallographic symmetry (NCS) with GETAX (Vornhein & Schulz, 1999). Density modification, solvent flattening, histogram-matching, NCS averaging and phase extension were performed with DM (Cowtan, 1994). Masks were generated and processed with NCSMASK (Collaborative Computational Project, Number 4, 1994) and MAMA (Kleywegt & Jones, 1999). *O* (Jones *et al.*, 1991) was used for the visual inspection of $(2F_o - F_c)$ and $(F_o - F_c)$ maps and for model building. The refinement was started with X-PLOR (Brünger, 1992) and later continued with REFMAC (Murshudov *et al.*, 1997) applying the bulk-solvent correction of X-PLOR (Jiang & Brünger, 1994). Water molecules were automatically gener-

ated using *ARPP* (Lamzin & Wilson, 1993) and sorted on the basis of NCS with *SORTWATER* (Collaborative Computational Project, Number 4, 1994). Figures were drawn using *MOLSCRIPT* (Kraulis, 1991), *Raster3D* (Merritt & Bacon, 1997) and *O* (Jones *et al.*, 1991).

3. Results and discussion

3.1. Similarity to FucA and working hypothesis

A sequence alignment of the 274 amino-acid residues of RhuA with the 215 residues of FucA resulted in 43 identical amino-acid residues (Fig. 2), including the most important active-centre residues of FucA (Joerger *et al.*, 2000). Moreover, the secondary-structure prediction of RhuA and the known secondary structure of FucA showed consensus in the central β -sheet and in the surrounding α -helices. Given this correspondence, we concluded that the chain folds of RhuA and FucA are probably similar. A closer inspection of Fig. 2 showed that 21 of the 43 identical residues were at the tetramer interface of FucA. Moreover, the catalytic centre of FucA is shared between two subunits. This observation indicates that RhuA and FucA not only have similar chain folds but also similar quarternary structures. Consequently, we put forward the working hypothesis that the RhuA tetramer obeys C_4 symmetry like the FucA tetramer and that the molecular envelopes are similar because the chain folds and the subunit interfaces are related to each other.

3.2. Crystals and self-rotation function

RhuA crystals have a large unit cell and belong to space group $P3_221$ (Table 1). Common crystal-packing statistics (Matthews, 1977) point to four to seven tetramers (16–28 protomers) in the asymmetric unit, corresponding to V_M values ranging from 4.5 to 2.6 $\text{\AA}^3 \text{Da}^{-1}$. Under the polarizing microscope the crystals showed birefringence along the crystallographic threefold screw axis, although trigonal packings should be isotropic along their main axis (Blundell & Johnson,

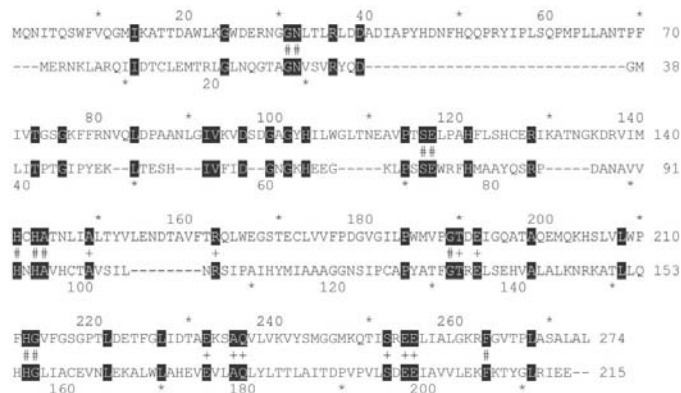


Figure 2 Sequence alignment of RhuA (top) with FucA (bottom). The conserved residues corresponding to the active centre (#) and the oligomer interface (+) of FucA are indicated. All of them were within 8 \AA distance of an atom of a neighbouring subunit of FucA. The sequence alignment agrees with the structural superposition shown in Fig. 9.

Table 1 Data-collection statistics.

Data set	Native-1†	Native-2‡	Ta ₆ Br ₁₂ ²⁺ †
Values in parentheses refer to the outermost resolution shell.			
Unit-cell parameters (\AA)			
$a = b$ (\AA)	229.0	225.8	228.5
c (\AA)	287.9	285.7	288.5
Resolution (\AA)	50–3.4 (3.6–3.4)	45–2.7 (2.8–2.7)	35–6.0 (6.3–6.0)
Total observations	173254	611276	50052
Unique reflections	96092	207606	19435
Completeness (%)	80 (52)	91 (90)	88 (78)
Average $I/\sigma(I)$	10.1 (4.2)	7.8 (2.1)	11.0 (6.1)
Redundancy	1.8 (1.2)	2.9 (2.6)	2.6 (1.9)
R_{sym}^{\S} (%)	6.9 (17)	8.9 (37)	6.3 (12)

† Data sets collected from a single crystal using Cu $K\alpha$ radiation from a rotating anode with a multiwire area detector at room temperature. ‡ Data set collected from a single crystal using 0.908 \AA wavelength synchrotron radiation at the EMBL Outstation (DESY, Hamburg). § $R_{\text{sym}} = \sum_{hkl,i} |I_{hkl,i} - \langle I_{hkl,i} \rangle| / \sum_{hkl,i} I_{hkl,i}$, where hkl stands for the hkl of unique reflections and i counts symmetry-related reflections.

1976). The largest, nearly square, crystal face was split into two pairs of triangles. The same optical effect had been observed with FucA (Dreyer & Schulz, 1996b). The data-collection statistics are summarized in Table 1.

For entropic reasons, the large number of protomers in the asymmetric unit should possess local symmetry. The self-rotation function indicated that there are indeed numerous local axes (Fig. 3). The map section at polar angle $\kappa = 90^\circ$ showed two fourfold axes, which were located on the mirror planes at $\varphi = 30, 150$ and 270° of this function and were therefore possibly amplified. Peak *A* at $(\omega, \varphi) = (7, 30^\circ)$ was as high as 3σ and peak *B* at $(26, 30^\circ)$ was 2σ . Among the numerous twofold axes observed in the $\kappa = 180^\circ$ section there was one peak system *A* that combined four 45° -spaced twofold axes with a perpendicular fourfold axis *A* transferred from the $\kappa = 90^\circ$ section. The fourfold axis causes a peak in the $\kappa = 180^\circ$ section because it is also twofold. Consequently, system *A* was likely to correspond to a D_4 -symmetric octamer which could consist of two FucA-like C_4 tetramers. Transferring the fourfold axis *B* to the $\kappa = 180^\circ$ section, however, did not allow the unambiguous assignment of a similar system of four 45° -spaced twofold axes because there were too many peaks to choose from (Fig. 3b).

3.3. Initial phasing

An early attempt to phase the reflections by molecular replacement using either a protomer or a tetramer of FucA as the search model failed. This was expected in view of the low sequence identity and the large unit cell. Therefore, we tried the isomorphous replacement method using Ta₆Br₁₂²⁺, which forms a regular octahedron of 4.3 \AA radius with 856 electrons and has been employed in a number of structural analyses (Knäblein *et al.*, 1997; Seemann & Schulz, 1997; Gomis-Rüth & Coll, 2001), as the modifying compound. Unfortunately, the derivative data could only be measured to 6 \AA resolution and no cluster orientation could be determined. Accordingly, we interpreted the 18 cluster atoms as a smeared-out single atom.

Although soaking with $\text{Ta}_6\text{Br}_{12}^{2+}$ is usually accompanied by intensive green coloration, the crystal of RhuA remained essentially colourless. However, the 6 Å resolution difference Patterson map showed a clear peak system at 13σ in the

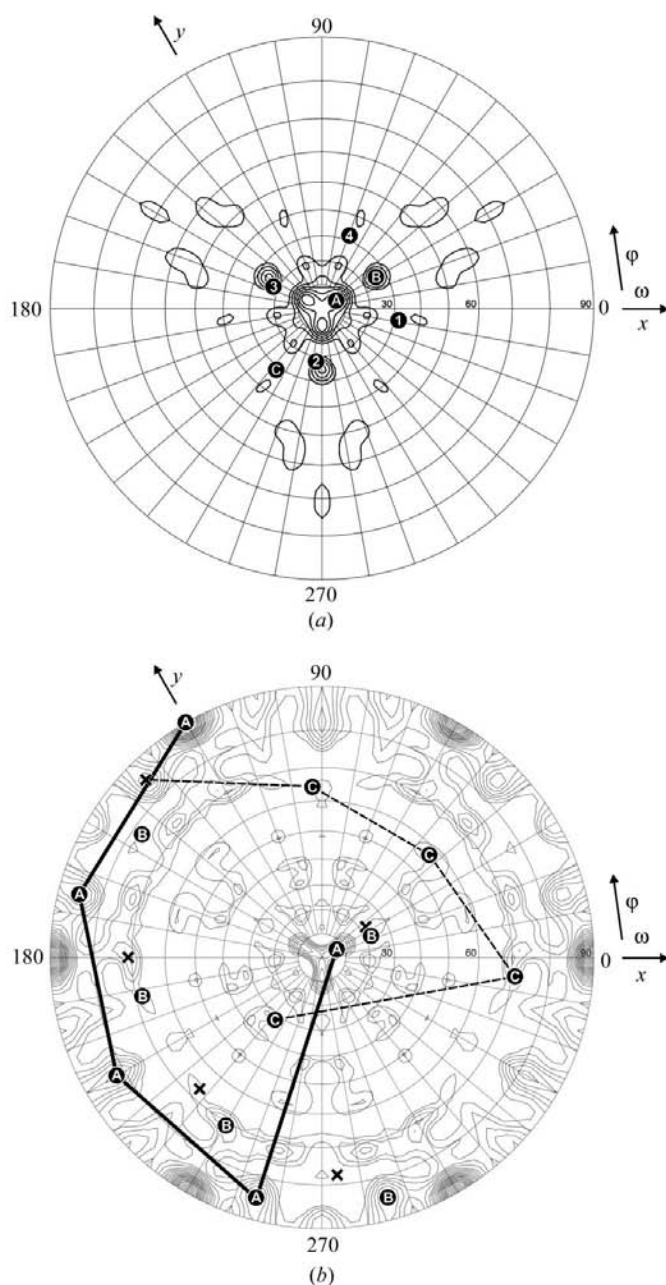


Figure 3

Stereographic projection of the self-rotation function of RhuA crystals (space group $P3_221$) calculated using data in the resolution range 8–6 Å and an integration radius from 5 to 35 Å. (a) The $\kappa = 90^\circ$ section, reporting fourfold axes with contour levels of 0.5, 1.0 σ etc. Two significant peaks at $(\omega, \varphi) = (7, 30^\circ)$ and $(26, 30^\circ)$ are marked A and B, respectively; peak C was derived from the $\kappa = 180^\circ$ section. The labels 1 to 4 show the orientation of the internal fourfold axes of the four propeller-blade octamers of the $z = 1/3$ layer. (b) The $\kappa = 180^\circ$ section is contoured at 1.5, 2.0 σ etc. Peak A of the $\kappa = 90^\circ$ section (near the pole) and four 45°-spaced twofold axes perpendicular to it are likely to arise from a D_4 -symmetric RhuA octamer. Peak B of the $\kappa = 90^\circ$ section split into the octamers B and B' (x) on density-averaging/NCS refinement. Octamer C detected in the third successful density-correlation search with *GETAX* is marked.

Table 2

Parameters of the $\text{Ta}_6\text{Br}_{12}^{2+}$ derivative.

R_{iso}^\dagger (%)	12.4
Position x, y, z^\ddagger	0.762, 0.270, 0.914
Figure of merit	0.26
Phasing power	0.96
R_{Cullis}^\S	0.85
$ \varphi_{\text{SIR}} - \varphi_{\text{refined}} ^\P$ (°)	74.2

$^\dagger R_{\text{iso}} = \sum_{hkl} |F_{PH} - F_P| / \sum_{hkl} |F_P|$, using the structure-factor amplitudes of native and derivative data. ‡ The B factor was set to 200 Å² to account for the spatial extension and the unknown orientation of the nearly octahedral tantalum cluster.

$^\S R_{\text{Cullis}} = \sum_{hkl} |F_{PH} - F_P| - F_H / \sum |F_{PH} - F_P|$, using the observed structure-factor amplitudes F_{PH} and F_P and the calculated heavy-atom contribution F_H . ¶ Calculated in retrospect: mean difference between the SIR phases and the final refined phases.

Harker section and in the $w = 0.17$ plane which arose from a single site. A difference Fourier synthesis revealed no second site. Obviously, the cluster was bound at only one particular corner of this complicated packing arrangement (see below). The $\text{Ta}_6\text{Br}_{12}^{2+}$ site was refined and used for phasing (Table 2). At a figure of merit of 0.26, the resulting single isomorphous replacement (SIR) phases were rather inaccurate. The corresponding map was then processed by solvent flattening and histogram matching in the 40–6 Å resolution range. For this purpose, we assumed a solvent content of 55%, which is somewhat below the average solvent content of 58% for large protein molecules (Matthews, 1977). The resulting 6 Å resolution map is illustrated in Fig. 4(a). It failed to reveal the molecular envelope of any of the expected tetramers or octamers.

3.4. Non-crystallographic symmetry and density modification

This first map was used for a real-space correlation search with *GETAX*, looking for local rotational symmetry within a defined cylinder around a given rotation axis. We used a cylinder with a radius of 50 Å and a height of 30 Å, which is somewhat larger than the FucA tetramer, and tried to find a fourfold rotation axis, in both respects following our working hypothesis. The *GETAX* search started with the axis orientation $(\omega, \varphi) = (7, 30^\circ)$ of the most significant peak A of Fig. 3(a), stepped through the whole unit cell and established a very clear correlation maximum. The corresponding local fourfold axis intersected a perpendicular crystallographic twofold axis running at $z = 1/3$ along the y axis (Fig. 5a), i.e. in the same direction $(\omega, \varphi) = (90, 120^\circ)$ as one of the twofold axes of peak system A (Fig. 3b). The local fourfold and the crystallographic twofold axes combined to form point group D_4 and thus confirmed our interpretation of peak system A in terms of a D_4 octamer. Next, we tackled peak B of the self-rotation function (Fig. 3a) in a second *GETAX* search. The orientation of the fourfold axis was $(\omega, \varphi) = (26, 30^\circ)$ and the cylinder was the same as in the first search. The resulting correlation map was rather noisy, but revealed a clear maximum identifying a second tetramer in the asymmetric unit (Fig. 5b).

At this point, we refined our working hypothesis and assumed that in the crystal all RhuA tetramers are associated in D_4 octamers as in the established octamer A, because we

felt that the oligomeric state was probably uniform for a given crystallization condition. This assumption was corroborated by numerous peaks in the $\kappa = 180^\circ$ section of the self-rotation function (Fig. 3*b*) that were perpendicular to the fourfold axis *B* and in more general terms also by the fact that a higher local symmetry is entropically more favourable. For producing a tentative mask of such an octamer, we first derived a tetramer mask from the known FucA structure (Dreyer & Schulz, 1993), placed it at the position of the *GETAX* solution *A* and doubled it by a rotation around the crystallographic twofold axis. The resulting octamer mask was then duplicated and placed at the *GETAX* solution *B*. The mask was centred in the 2σ contour which formed a 'cigar' of appropriate length around *B*. The 2σ contour is not shown in Fig. 5(*b*), which for clarity was drawn at the 3.5σ level.

The octamer mask at *GETAX* solution *B* and the (crystallographically asymmetric) tetramer mask at solution *A* were then used for density averaging/NCS refinement with *DM*. The refinement tilted the axis of system *A* by less than 1° , but tilted the axis of system *B* by as much as 5° , thus splitting the original peak *B* on the mirror plane ($\varphi = 30^\circ$) of the self-rotation function (Fig. 3*a*) into the mirror-related peaks *B* and *B'* shown in Fig. 3(*b*). The resulting electron-density map was slightly improved, but the three located RhuA tetramers (one

in *A* and two in *B*) did not fill the asymmetric unit. Therefore, we continued the *GETAX* searches with the improved density map. First, we checked all other peaks of the $\kappa = 90^\circ$ section of the self-rotation function and then all peaks of the $\kappa = 180^\circ$ section because these could also represent fourfold axes. Eventually, we detected the very significant density-correlation peak *C* (Fig. 5*c*) which was surrounded by enough free space for a further D_4 octamer in the asymmetric unit. This octamer filled up the unit cell, giving rise to a reasonable packing parameter of $3.6 \text{ \AA}^3 \text{ Da}^{-1}$ (Matthews, 1977).

Subsequently, we returned to *DM* and defined a fixed solvent mask as comprising the 61% solvent outside all octamer masks. Further density averaging within the two and a half octamer masks of the asymmetric unit resulted in the largely improved 6 \AA resolution electron-density map depicted in Fig. 4(*b*), which permitted determination of the outline of the RhuA protomer and the production of a genuine RhuA protomer mask. Using this mask, we backed up to 8.5 \AA resolution and started a new round of density averaging/NCS refinement and included a phase extension. This procedure reached the 3.4 \AA resolution limit of data set Native-1, yielding a map suitable for model building (Fig. 4*c*), again demonstrating the power of density averaging for an extensive (in this case 20-fold) NCS (Kleywegt & Read, 1997).

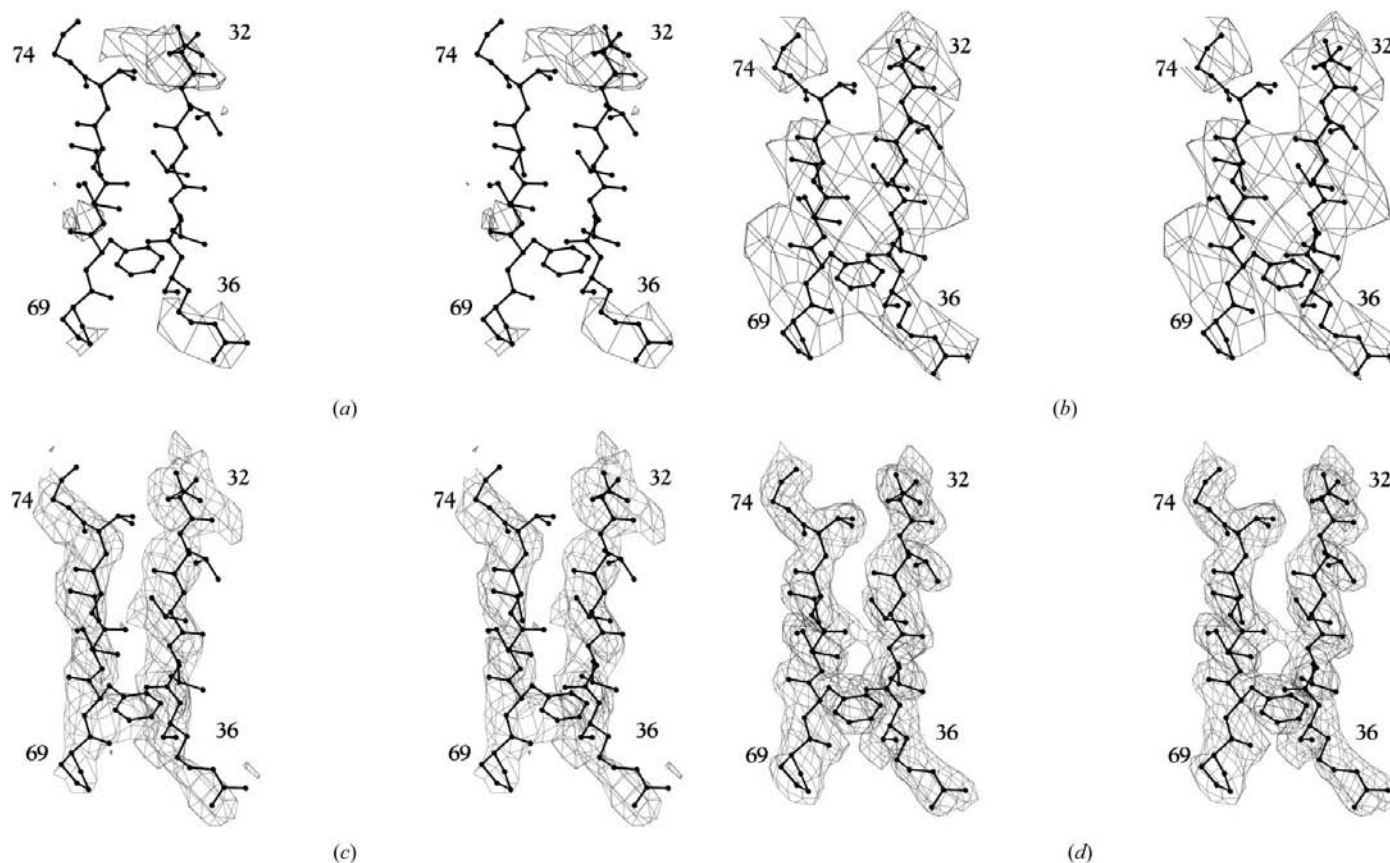


Figure 4

Phasing progress as demonstrated by the electron-density maps at the 1σ level in the region of the central β -sheet. The final model (residues 32–36 and 69–74) is given as a frame of reference. (*a*) Initial solvent-flattened SIR map at 6.0 \AA resolution used in the first two density-correlation searches. (*b*) Final averaged map after establishing the 20-fold NCS at 6.0 \AA resolution. (*c*) Solvent-flattened, NCS-averaged and phase-extended map at 3.4 \AA resolution. (*d*) Final $(2F_o - F_c)$ map at 2.7 \AA resolution.

3.5. Model building and refinement

The resulting 3.4 Å resolution map (Fig. 4c) was used to build an initial model of RhuA, which was subsequently refined to an R factor of 30% with *X-PLOR*. After that, a second data set Native-2 was collected and refinement was continued with *REFMAC* to the 2.7 Å resolution limit, yielding an R factor of 23.3% (Table 3). Restrained individual isotropic B factors were calculated in every refinement cycle and the bulk-solvent correction of *X-PLOR* was used. The 20-fold NCS was always tightly restrained, even near the crystal contacts. The final density map is illustrated in Fig. 4(d).

All 274 residues of the RhuA protomer were clearly visible in the electron-density map, with the exception of a surface loop consisting of residues 50–53. This loop participated in crystal contacts and the corresponding density was therefore

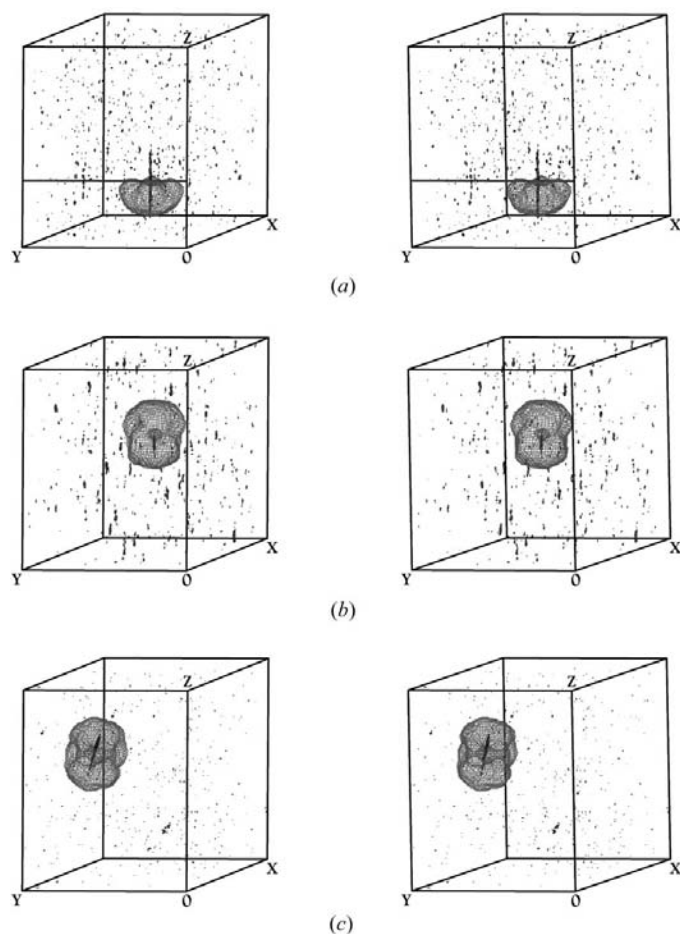


Figure 5

Density-correlation search for local fourfold symmetry axes using program *GETAX*, which averages locally along the given axis orientation. The range was a cylinder with 50 Å radius and 30 Å height approximating the FucA tetramer. Depicted are the octamer masks produced from two FucA tetramer masks that were used for density averaging/NCS refinement. (a) Correlation search at $(\omega, \varphi) = (7, 30^\circ)$. The local fourfold axis perpendicularly intersects the crystallographic twofold axis at $z = 1/3$, establishing octamer A. (b) Search at $(\omega, \varphi) = (26, 30^\circ)$ showing the precursor of octamers B and B'. The split into B and B' occurred through NCS refinement. (c) Search at $(\omega, \varphi) = (33, 233^\circ)$ yielding octamer C.

Table 3

Refinement statistics of data set Native-2.

Resolution range (Å)	44–2.7
Unique reflections	207386
Refined atoms†	
Total	46180 (40)
Protein	42480 (40)
Phosphoglycolhydroxamate	200 (52)
Zinc	20 (34)
Water	3480 (43)
R factor‡ (%)	23.3
Free R factor§ (%)	23.5

† Accounting for 20 protomers in the crystallographic asymmetric unit. The average B factors (Å²) are given in parentheses. The root-mean-square deviation between NCS-related atoms was 0.036 Å. ‡ The root-mean-square-deviations of bond lengths and angles were 0.016 and 0.037 Å, respectively. Those of the B factors of bond-related, angle-related and NCS-related atoms were 1.42, 2.42 and 0.07 Å², respectively. The Ramachandran plot showed 90.0 and 9.6% of the non-glycine non-proline residues in 'most favoured' and 'additionally allowed' regions. Only Arg28 was in a forbidden region (Laskowski *et al.*, 1993). § The free R factor was based on a random test set containing 1036 reflections. It is almost meaningless because the extensive NCS introduces a strong interdependence between all reflections.

destroyed by the NCS averaging. Water molecules were automatically generated using *ARPP*, but only 174 water molecules obeying the 20-fold NCS were retained. This number is in the usual range for the given resolution and protein size.

3.6. Packing arrangement

The NCS seemed to be extremely complex when we established it piece by piece. After the refinement, however, the packing arrangement turned out to be rather simple. When projecting the electron-density map onto the threefold screw

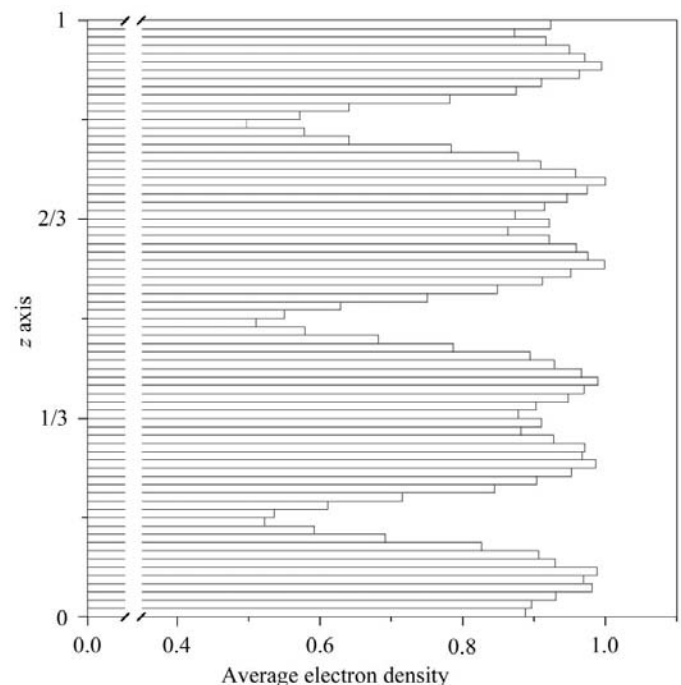


Figure 6

Projection of the F_{calc} -based electron-density map of one unit cell onto the axis. The density minima at $z = 1/6, 1/2$ and $5/6$ separate three layers of RhuA octamers, which in turn are split into pairs of tetramer layers as indicated by the double-headed peak distributions.

axes z , we found pronounced layers centred at z levels 0, 1/3 and 2/3 (Fig. 6). The structure of the $z = 1/3$ layer is depicted in Fig. 7. It contains five octamers per unit cell that form a propeller centred at the point $(x, y, z) = (0, 0.218, 1/3)$. The tantalum clusters were bound at the lateral contacts, extending the propellers over the whole plane. The other layers are identical but rotated by 120° around the crystallographic 3_2 axis. They pile up to form the crystal.

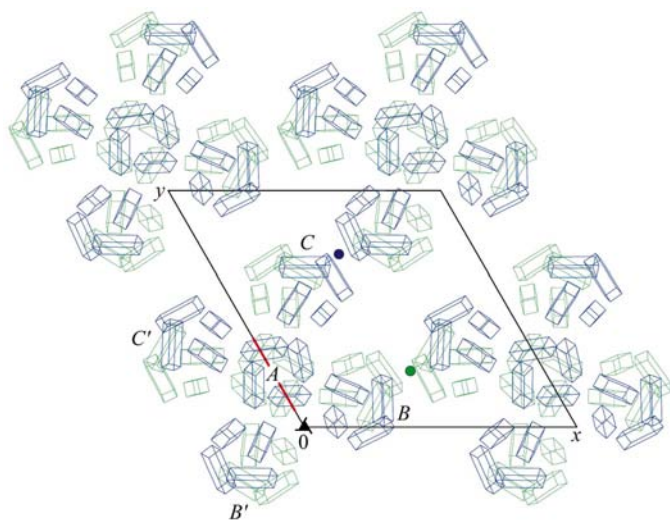


Figure 7

Crystal packing of RhuA showing the $z = 1/3$ layer in space group $P3_221$. The layer is assembled from D_4 -symmetric propellers each containing five octamers or 40 protomers. The propeller encloses a crystallographic twofold axis (red, $z = 1/3$), so that the asymmetric unit contains 20 protomers. The propeller axis is tilted by 7° against the 3_2 axis. All four propeller blades consist of octamers with an internal D_4 symmetry. All other layers of the crystals are generated by the 3_2 symmetry axis along z . Octamers A (tetramer in the asymmetric unit), B and C identified in the self-rotation function (Fig. 3) are labelled, together with their crystallographically related partners B' and C' . The tantalum cluster (dot) was bound at the contacts connecting the propellers within a layer.

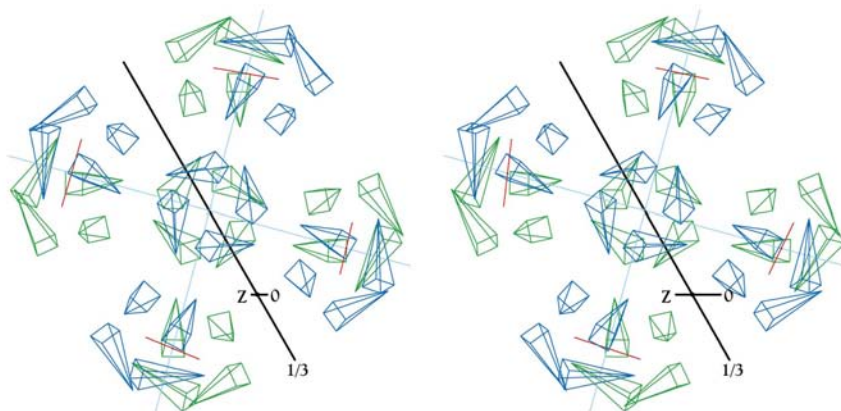


Figure 8

Stereoview of a propeller consisting of five octamers. The view is along the propeller axis which deviates by 7° from the z axis (depicted). The crystallographic twofold axis at $z = 1/3$ is indicated by a thick line. The fourfold and twofold axes of the D_4 -symmetric propeller are in blue. Each blade shows a lower level D_4 symmetry, with one twofold axis (blue) coinciding with the propeller twofold. The fourfold axes of the blades are in red.

The propeller shows D_4 symmetry, with one of the twofold axes coinciding with a crystallographic twofold axis (Fig. 8). Its fourfold axis and thus the whole propeller is tilted by 7° from the z axis. The octamer in each propeller blade has a lower level D_4 symmetry concerning only this particular blade. With their high internal symmetry, the propellers should be considered as the basic building blocks of the crystal. Compared with a disordered packing of five tetramers in the asymmetric unit, pre-association into the propellers reduces the entropy loss on crystallization appreciably. Since a low entropy loss is required for facile crystallization, we suggest that the propellers are indeed preformed at the crystallization conditions. Under normal conditions in solution, however, there is no indication that RhuA forms aggregates larger than tetramers.

It seems worthwhile to review the self-rotation function (Fig. 3) in the light of the propeller symmetry. Peak system A is dominant because it corresponds to the whole propeller. Lacking this knowledge, however, we interpreted it merely as the hub octamer A (Fig. 5a). The density-correlation search with peak B revealed an octamer in the $z = 2/3$ layer (Fig. 5b) that split into the crystallographically related blade octamers B and B' (Fig. 7). Octamer C of the $z = 2/3$ layer (Fig. 5c) was detected when checking through the remaining peaks of the self-rotation function. It was then transferred to the crystallographically related blade octamers C and C' of the $z = 1/3$ layer (Fig. 7). The four fourfold axes of the blade octamers of the $z = 1/3$ layer propeller are marked in Fig. 3(a).

3.7. Structure description

The quality of the model obtained is reasonable (Table 3). The only residue in a forbidden (but glycine-allowed) region of the Ramachandran plot is Arg28 in the active centre near the phosphate of DHAP. This residue corresponds to a glycine in FucA (Fig. 2). A superposition of the C^α -chain folds of RhuA and FucA in Fig. 9 showed good agreement, quantified by the observation that 136 C^α atoms were superimposed within the commonly applied 3 Å cutoff. The sequence alignment of Fig. 2 agrees with the structure alignment. Moreover, the chain-fold superposition brings the molecular fourfold axes close together. This confirms the working hypothesis, which played a crucial role in the establishment of the NCS and thus in the structure analysis.

As expected from the sequence alignment (Fig. 2), the active-centre structures around the Zn^{2+} ion resemble each other with respect to the four nearest zinc ligands, which consist of three histidines and a glutamic acid. Interestingly, the fifth zinc ligand, which is at a longer distance and comes from the neighbouring subunit, varies between the tyrosine of FucA and the threonine of RhuA. Such a geometric difference should be expected because L-rhamnulose-1-phosphate

is the 4-epimer of L-fuculose-1-phosphate. The binding mode of the inhibitor phosphoglycolohydroxamate was the same in RhuA as in FucA, in agreement with the fact that it mimics the common substrate DHAP of these two enzymes (Fig. 1).

A ribbon plot of the RhuA tetramer is depicted in Fig. 10. The solvent-accessible surface (SAS) buried on tetramer formation is 2800 \AA^2 per subunit (23.5%, subunit SAS = $11\,900 \text{ \AA}^2$). This is a typical large oligomer interface area. The formation of the octamer by two tetramers buries a further 3050 \AA^2 per tetramer (8.4%, tetramer SAS = $36\,350 \text{ \AA}^2$), which corresponds to a large crystal contact. In agreement with the commonly observed RhuA tetramer in solution, however, it is too small for an oligomeric interface. The active centres are indicated by the zinc ions and the inhibitors. They are located in deep clefts at the interfaces between two subunits.

The chain fold of a single subunit contains a central nine-stranded β -pleated sheet. Except for the two parallel strands $\beta 7$ and $\beta 8$, the sheet is antiparallel and sandwiched between two layers of helices. The overall structure of RhuA resembles the structure of the homologous FucA (Dreyer & Schulz, 1993). In contrast to FucA, however, the C-terminal α -helix does not point towards the active centre of a neighbouring subunit within the tetramer, but is fixed by hydrogen bonds to the same subunit. Moreover, it is completely defined in the electron-density map, establishing another substantial structural difference likely to affect the stereochemistry of the reaction. The structure presented can be used for a further analysis of the catalyzed reaction.

We thank G. Sinerius and W. D. Fessner for the expression plasmid, J. V. Schloss and M. Hixon for phosphoglycolohydroxamate and R. Huber for tantalum bromide. Moreover, we thank the team of the EMBL Outstation, Hamburg for help in data collection at the synchrotron. The support of the Bundesministerium für Bildung und Forschung BMBF under BEO/31-0310898 is acknowledged.

References

Blom, N. S. & Sygusch, J. (1997). *Nature Struct. Biol.* **4**, 36–39.
 Bednarski, M. D., Simon, E. S., Bischofberger, N., Fessner, W.-D., Kim, M.-J., Lees, W., Saito, T., Waldmann, H. & Whitesides, G. M. (1989). *J. Am. Chem. Soc.* **111**, 627–635.

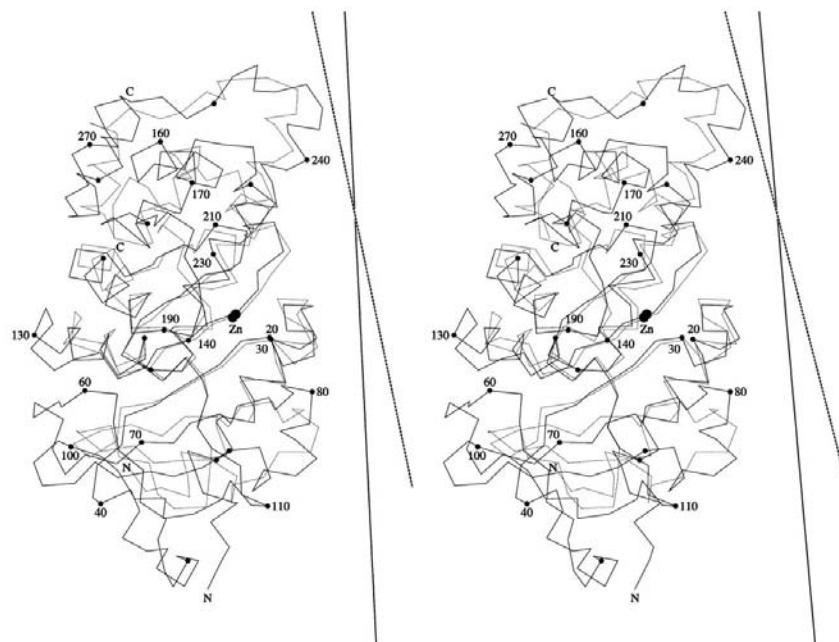


Figure 9

Superposition of the C^α chain folds of one subunit of RhuA (solid lines) and one subunit of FucA (dotted lines; PDB code 4fua). The structure alignment confirms the sequence alignment shown in Fig. 2: residues 8–37, 70–79, 113–129, 135–151, 171–173 and 180–238 of RhuA superpose within 3 \AA with residues 5–34, 38–47, 69–85, 86–102, 114–116 and 123–181 of FucA, respectively. The molecular fourfold axes are shown.

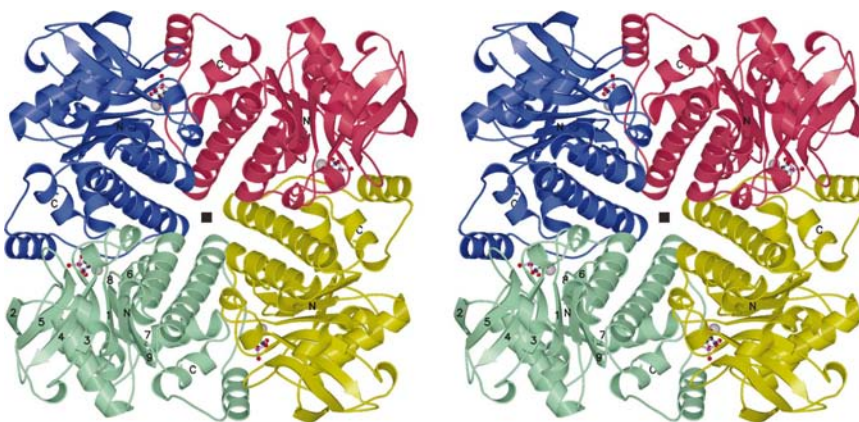


Figure 10

Stereoview along the fourfold axis of the RhuA tetramer showing the C_4 symmetry. The zinc ions are shown as spheres and the phosphoglycolohydroxamate inhibitors occupying the DHAP sites (Joerger *et al.*, 2000) as a ball-and-stick models. The N- and C-termini and the β -strand numbers are given. The active centres are between subunits.

Blundell, T. L. & Johnson, L. N. (1976). *Protein Crystallography*, pp. 97–104. New York: Academic Press.

Brünger, A. T. (1992). *X-PLOR Version 3.1. A System for X-ray Crystallography and NMR*. New Haven: Yale University Press.

Chiu, T.-H. & Feingold, D. S. (1969). *Biochemistry*, **8**, 98–108.

Collaborative Computational Project, Number 4 (1994). *Acta Cryst.* **D50**, 760–763.

Cooper, S. J., Leonard, G. A., McSweeney, S. M., Thompson, A. W., Naismith, J. H., Qamar, S., Plater, A., Berry, A. & Hunter, W. N. (1996). *Structure*, **4**, 1303–1315.

Cowan, K. D. (1994). *Jnt CCP4/ESF-EACBM Newsl. Protein Crystallogr.* **31**, 34–38.

Dalby, A. R., Tolan, D. R. & Littlechild, J. A. (2001). *Acta Cryst.* **D57**,

- 1526–1533.
- Dreyer, M. K. & Schulz, G. E. (1993). *J. Mol. Biol.* **231**, 549–553.
- Dreyer, M. K. & Schulz, G. E. (1996a). *J. Mol. Biol.* **259**, 458–466.
- Dreyer, M. K. & Schulz, G. E. (1996b). *Acta Cryst.* **D52**, 1082–1091.
- Evans, P. R. (1993). *Proceedings of the CCP4 Study Weekend. Data Collection and Processing*, edited by L. Sawyer, N. Isaacs & S. Bailey, pp. 114–122. Warrington: Daresbury Laboratory.
- Fessner, W.-D., Sinerius, G., Schneider, A., Dreyer, M., Schulz, G. E., Badia, J. & Aguilar, J. (1991). *Angew. Chem. Int. Ed. Engl.* **30**, 555–558.
- Fessner, W.-D. & Walter, C. (1996). *Top. Curr. Chem.* **184**, 97–194.
- Gomis-Rüth, F.-X. & Coll, M. (2001). *Acta Cryst.* **D57**, 800–805.
- Horecker, B. L., Tsolas, O. & Lai, C. Y. (1972). *The Enzymes*, 3rd ed, edited by P. D. Boyer, Vol. 7, pp. 213–258. New York: Academic Press.
- Howell, P. L. & Smith, G. D. (1992). *J. Appl. Cryst.* **25**, 81–86.
- Izard, T. & Blackwell, N. C. (2000). *EMBO J.* **19**, 3849–3856.
- Jancarik, J. & Kim, S.-H. (1991). *J. Appl. Cryst.* **24**, 409–411.
- Jiang, J.-S. & Brünger, A. T. (1994). *J. Mol. Biol.* **243**, 100–115.
- Joerger, A. C., Mueller-Dieckmann, C. & Schulz, G. E. (2000). *J. Mol. Biol.* **303**, 531–543.
- Jones, T. A., Zou, J.-Y., Cowan, S. W. & Kjeldgaard, M. (1991). *Acta Cryst.* **A47**, 110–119.
- Kabsch, W. (1988). *J. Appl. Cryst.* **21**, 916–924.
- Kim, H., Certa, U., Döbeli, H., Jakob, P. & Hol, W. G. J. (1998). *Biochemistry*, **37**, 4388–4396.
- Kleywegt, G. J. & Jones, T. A. (1999). *Acta Cryst.* **D55**, 941–944.
- Kleywegt, G. J. & Read, R. J. (1997). *Structure*, **5**, 1557–1569.
- Knäblein, J., Neufeind, T., Schneider, F., Bergner, A., Messerschmidt, A., Löwe, J., Steipe, B. & Huber, R. (1997). *J. Mol. Biol.* **270**, 1–7.
- Kraulis, P. J. (1991). *J. Appl. Cryst.* **24**, 946–950.
- Lamzin, V. S. & Wilson, K. S. (1993). *Acta Cryst.* **D49**, 129–147.
- Laskowski, R. A., MacArthur, M. W., Moss, D. S. & Thornton, J. M. (1993). *J. Appl. Cryst.* **26**, 283–291.
- Leslie, A. G. W. (1992). *Jnt CCP4/ESF-EAMCB Newsl. Protein Crystallogr.* **26**.
- Matthews, B. W. (1977). *The Proteins*, 3rd ed, edited by H. Neurath & R. L. Hill, pp. 404–590. New York: Academic Press.
- Merritt, E. A. & Bacon, D. J. (1997). *Methods Enzymol.* **277**, 505–524.
- Moralejo, P., Egan, S. M., Hidalgo, E. & Aguilar, J. (1993). *J. Bacteriol.* **175**, 5585–5594.
- Murshudov, G. N., Vagin, A. A. & Dodson, E. J. (1997). *Acta Cryst.* **D53**, 240–255.
- Seemann, J. E. & Schulz, G. E. (1997). *J. Mol. Biol.* **273**, 256–268.
- Vonrhein, C. & Schulz, G. E. (1999). *Acta Cryst.* **D55**, 225–229.
- Wong, C.-H., Halcomb, R. L., Ichikawa, Y. & Kajimoto, T. (1995). *Angew. Chem. Int. Ed. Engl.* **34**, 412–432.
- Wymer, N., Buchanan, L. V., Henderson, D., Mehta, N., Botting, C. H., Pocivavsek, L., Fierke, C. A., Toone, E. J. & Naismith, J. H. (2001). *Structure*, **9**, 1–9.